

The Crab Nebula at 1.3 mm

Evidence for a new synchrotron component^{*}

R. Bandiera¹, R. Neri², and R. Cesaroni³

¹ Osservatorio Astrofisico di Arcetri, Largo E. Fermi 5, 50125 Firenze, Italy

² IRAM, 300 rue de la Piscine, 38406 St Martin d'Hères, France
e-mail: neri@iram.fr

³ Osservatorio Astrofisico di Arcetri, Largo E. Fermi 5, 50125 Firenze, Italy
e-mail: cesa@arcetri.astro.it

Received 19 December 2001 / Accepted 28 February 2002

Abstract. We present the results of 1.3 mm observations of the Crab Nebula, performed with the MPIfR bolometer arrays at the IRAM 30-m telescope. The maps obtained, of unprecedented quality at these wavelengths, allow a direct comparison with high-resolution radio maps. Although the spatial structure of the Crab Nebula does not change much from radio to millimetre wavelengths, we have detected significant spatial variations of the spectral index between 20 cm and 1.3 mm. The main effect is a spectral flattening in the inner region, which can be hardly explained just in terms of the evolution of a single population of synchrotron emitting electrons. We propose instead that this is the result of the emergence of a second synchrotron component, that we have tried to extract from the data. Shape and size of this component resemble those of the Crab Nebula in X-rays. However, while the more compact structure of the Crab Nebula in X-rays is commonly regarded as an effect of synchrotron downgrading, it cannot be explained why a similar structure is present also at millimetre wavelengths, where the electron lifetimes far exceed the nebular age. Our data, combined with published upper limits on spatial variations of the radio spectral index, also imply a low-energy cutoff for the distribution of electrons responsible for this additional synchrotron component. Although no model has been developed so far to explain the details of this component, one may verify that the total number of the electrons responsible for it is in agreement with what predicted by the classical pulsar-wind models, which otherwise are known to fail in accounting for the number of radio emitting electrons. This numerical coincidence can give indications about the origin of this component. We have also detected a spectral steepening at millimetre wavelengths in some elongated regions, whose positions match those of radio synchrotron filaments. The steepening is taken as the indication that magnetic fields in synchrotron filaments are stronger than the average nebular field.

Key words. ISM: individual objects: Crab Nebula – ISM: supernova remnants – radiation mechanisms: non-thermal – radio continuum: ISM

1. Introduction

The Crab Nebula is the prototype of synchrotron nebulae powered by a spinning-down pulsar, also known under the name of “plerions” (Weiler & Panagia 1978). This is an extensively studied object, and a wealth of information on the synchrotron nebula comes from detailed observations performed in various spectral ranges, like in radio, infrared, optical, UV and X-rays.

Send offprint requests to: R. Bandiera,
e-mail: bandiera@arcetri.astro.it

^{*} Based on observations carried out with the IRAM 30-m telescope located at Pico Veleta. IRAM is supported by INSU/CNRS (France), MPG (Germany) and IGN (Spain).

Modelling all the available data in a comprehensive frame represents a formidable task for the theory. Classical approaches to the modelling of the Crab synchrotron emission, like Pacini & Salvati (1973) and Kennel & Coroniti (1984a, 1984b), got some success. But more elaborate models can hardly get any substantial improvement with respect to the original approaches, partly because the geometric structure of the Crab Nebula is very complex, but probably also because the processes involved are not fully understood. When more quantitative and detailed modelling will be possible with other plerions we expect to face similar problems: in these respects a large part of the results on the Crab Nebula are likely to be exported to other objects.

Considering just the total luminosity spectrum, Pacini & Salvati (1973) successfully reproduced it from radio to optical, by simply assuming a pure power-law distribution for the injected “particles” (hereafter used to indicate relativistic electrons, as well as positrons): but in order to explain by their model the further spectral steepening in the X-ray range and beyond, an ad hoc spectrum for the injected particles is required. On the other hand Kennel & Coroniti (1984b) successfully reproduced the spectrum from optical to gamma rays, just assuming a power-law distribution (over a range of energies) for the particles accelerated at the termination shock of the pulsar relativistic wind. However their model fails in explaining the observed radio emission: the problem is that the best-fit wind model implies also an estimate of the total number of radio emitting particles injected into the nebula, which is at least a factor 100 lower than what measured. Up to now this discrepancy has been cured only by introducing some ad hoc assumptions (see e.g. Atoyan 1999).

As far as the spatial structure of the nebula is concerned, it is not difficult to explain qualitatively its behaviour with frequency, namely the shrinking of the nebular size with increasing frequency: in fact the latter corresponds to increasing particle energy, and therefore decreasing synchrotron lifetimes. However quantitative approaches fail to reproduce the observed profiles, both in the Kennel & Coroniti (1984b) and in the Pacini & Salvati (1973) frameworks: the implications of the assumptions in the latter paper on the nebular spatial extent have been investigated by Amato et al. (2000). A common characteristic of the above models is that the particles are advected outwards with the magnetic field, following the MHD equations. Somehow better results are for instance obtained by including also diffusive processes, but only when an ad hoc diffusion coefficient is taken.

An alternative to the above scenarios relies on assuming the coexistence of two (or more) components of injected particles, with different spectra as well as with different spatial locations. But one may be unwilling to increase the complexity of the models, unless a stringent evidence in that sense comes out from the observations. Since adiabatic losses preserve the slope of the particles distribution, the most direct test on the presence of multiple components of the injected particles consists into measuring spatial variations of the synchrotron spectral index that cannot in any way result from a synchrotron downgrading (i.e. the spectral softening consequent to synchrotron evolution of the emitting particles). This can be done observing at frequencies so low that the related particles are subject to negligible synchrotron losses, and therefore whose distribution retains the slope which had at the injection.

Beforehand this kind of test had been done only at radio wavelengths (below with the term “radio wavelengths” we roughly indicate wavelengths above 1 cm). Previous claims of spatial variations of the radio spectral index (Velusamy et al. 1992) have been then contradicted (Bietenholz et al. 1997). Possibly some variations of the

spectral index are present in the very central region, with scales of a few arcsec and associated to the “wisps” structures (Bietenholz & Kronberg 1992): however such result could be a mere artifact, originated by comparing data taken at different epochs, in the presence of rapidly moving wavy structures (Bietenholz et al. 2001). In fact recent radio observations (Bietenholz et al. 1997) strongly support the idea of a single injected distribution, by putting a tight upper limit, 0.01, to spatial variations of the spectral index, at least on scales larger than $16''$.

In this paper we will show that millimetric wavelengths represent the most appropriate spectral range to investigate this issue in the Crab Nebula, by providing new pieces of information with respect to the radio. The map presented in this paper, with a $10.5''$ resolution, is by far better than the only map of the Crab Nebula previously published at these wavelengths (Mezger et al. 1986, with only $120''$ resolution). The paper is organized as follows: in Sect. 2 we report on the observation parameters and on the data reduction; Sect. 3 describes the procedure by which our 1.3 mm map has been compared with a 20 cm radio map; features coming out from this comparison, namely the emergence of a second component in the inner regions and a general bending in filaments spectra, are respectively discussed in Sects. 4 and 5; Sect. 6 shows that the nature of the emission from the inner component is synchrotron; the morphology of the new synchrotron component is compared in Sect. 7 with maps at other wavelengths; in Sect. 8 we comment on possible spurious effects on our results deriving from time variability of the source; Sect. 9 concludes.

2. Observations

The Crab Nebula has been observed during two different runs at the 30-m telescope located at Pico Veleta (near Granada, Spain) and operated by the Institute de Radioastronomie Millimétrique (IRAM); to this purpose, we have used two different bolometer arrays (MAMBO) developed by the Max-Planck-Institut für Radioastronomie (MPIfR). In the former run (Dec. 2–3 1998), characterised by poor atmospheric conditions, we have mapped the source using the 19-element bolometer; while in the latter (Feb. 13–14 2000) we have obtained a map with the newly developed 37-element bolometer and with good atmospheric conditions.

In both the 19-element and the 37-element array the individual bolometers are organized in a hexagonal structure. The FWHP beamwidth of the telescope at 1.3 mm has been estimated from pointing scans on NRAO 530 and found to be $\sim 10''.5$. The frequency bandwidth ranges from 200 to about 280 GHz: the effective frequency of the observation varies slightly with the atmospheric opacity and with the spectral index of the source, and keeps typically in the range 230–240 GHz. A detailed description of the instruments may be found in Kreysa et al. (1998).

The maps have been obtained by on-the-fly scans in the dual-beam mode. The telescope scans the source in azimuth (at the velocity of $4''/s$, corresponding to a spatial

sampling of $2''$), while the secondary mirror is chopping, again in azimuth, at a frequency of 2 Hz with an elongation of $45''$. The shift in elevation between subsequent elementary scans is $4''$: in a complete raster scan each element of the bolometer then samples the whole source. Various slices of the Crab Nebula (4 for the December 1998 run; 8 for the February 2000 one) have been observed, each at a slightly different parallactic angle and center. To provide the best mapping coverage, the shape and size of the slices were continuously optimized during the observations. Redundant information was used to improve the signal-to-noise ratio, as well as to keep trace of the quality of the observations. The slices were gridded on a regular equatorial frame and finally combined according to their weights. In the February 2000 run the mapping sensitivity varies by a factor of two over the whole plerion: it is found to be highest close to the center, in the north and southeast. Outside the plerion, the rms noise sensitivity is about 6 mJy/beam .

The atmospheric zenith opacity has been monitored by repeating a skydip every hour. The flux calibration was performed on planets. The pointing was checked every hour on QSO B0528+134 and found to be better than $2''$. Given the superior quality of the data taken in February 2000 under good atmospheric conditions, in the following we will use only the resulting average map obtained with the 37-element bolometer array: this is shown in Fig. 1.

The map obtained in December 1988, though of poorer quality, has been used to check the accuracy of the absolute calibration. Though differences in the overall calibration have not shown up at levels above 10% between the December 1998 and February 2000 maps, we prefer to be more conservative and claim rather a 20% accuracy for the map of the Crab Nebula. This value also includes possible flux variations across the map (at a $\sim 200''$ scale) due to differential pickup emission between the on and off error-beams of the telescope, but is, according to simulations, by no means affecting quantitatively the relative accuracy at lower mapping scales. The relative accuracy across the map has independently been estimated also by comparison of two map slices taken under different observing conditions in February 2000 and turns out to be $\sim 10\%$.

The data have been reduced using the NIC package, which is part of the GAG software developed at IRAM and Observatoire de Grenoble.

3. Comparison with a 20 cm map

In this section we describe the procedure we have followed in order to estimate the difference between our 1.3 mm map and a reference radio map at lower frequency. Due to the high homogeneity of the spectral index over the radio nebula (Bietenholz et al. 1997) the choice of the reference radio frequency is not crucial. We have used a map of the radio continuum at 1.41 GHz, based on data taken at the NRAO Very Large Array (VLA), and kindly provided by

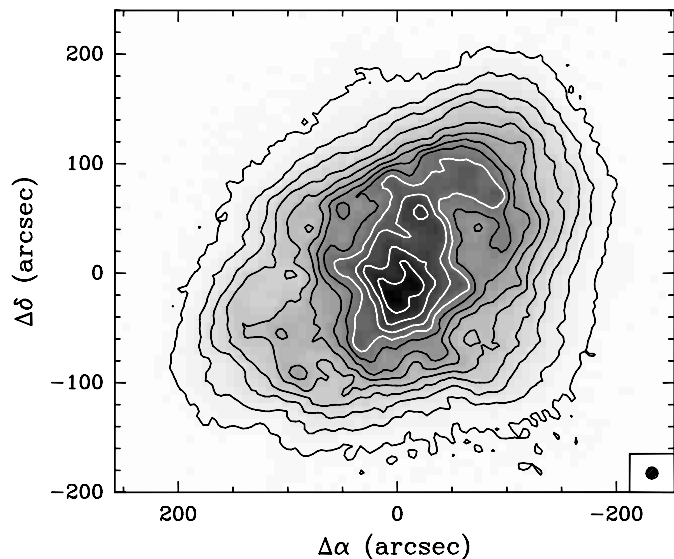


Fig. 1. Map of the Crab Nebula at 1.3 mm with $10''.5$ resolution. The contour levels range from 0.2 to 6.8 in steps of $0.6 \text{ mJy arcsec}^{-2}$.

M. F. Bietenholz. This is one of the highest-quality maps of the Crab Nebula produced so far in the radio range.

The VLA data, their analysis and the quality of the resulting map are described in detail by Bietenholz & Kronberg (1991). In short, the data have been collected with a series of runs in 1985–1986. The map has been produced by combining observations in all 4 VLA configurations: the cleaned beam size of this map is $2''.0 \times 1''.8$ and the u - v plane results very well sampled. Therefore this map (which is also corrected for primary mean attenuation) guarantees a high photometric accuracy also on large scales. The integrated flux in the cleaned map is 870 Jy, close to the expected 907 Jy: we have then increased by 4.3% the flux of this map, in order to correct for the small flux deficiency produced by residual gaps in the u - v coverage.

In order to allow an accurate comparison between maps taken at different epochs, we have first corrected the size and flux for the secular evolution. We have taken 1986 as the average date of the VLA map, and 2000 for our map: this time difference results into an estimated size difference of 1.9% (for an expansion time of 730 yr, Bietenholz et al. 1991) and a flux difference of -2.3% (for a fading rate of $-0.167\% \text{ yr}^{-1}$, Aller & Reynolds 1985). The total flux of the resulting radio map, extrapolated to year 2000, is then 886 Jy. We have finally convolved this image with a Gaussian function in order to obtain a $10''.5$ resolution map.

In the 1.3 mm map we have evaluated in $\simeq 5.5 \text{ mJy/beam}$ the average background level in the region external to the area covered by the Crab Nebula (where the boundaries of the nebula have been obtained from the smoothed radio map). This offset accounts for a flux of $\simeq 4.4 \text{ Jy}$ on the area covered by the nebula, and of $\simeq 21 \text{ Jy}$ over the total observed field: this is a small

quantity, in the sense that its presence does not change the qualitative scenario. However, in order to obtain more accurate quantitative results, we have subtracted this offset from the 1.3 mm map, by assuming that this background term is purely additive. After this correction the total flux of the Crab Nebula at 1.3 mm is estimated as $\simeq 260$ Jy (still taking 20% as a conservative estimate of the uncertainty in the absolute flux).

After this processing, at a first glance the maps at 1.3 mm and 20 cm look quite similar, but a quantitative comparison shows significant differences. The most standard way to outline such differences is generating a map of the spectral index (Fig. 2; where the spectral index α is defined by $F(\nu) \propto \nu^\alpha$).

The most apparent effect, in this map, is a flattening of the spectral index in the inner regions. The level of spectral index inhomogeneities is one order of magnitude larger than the upper limit put on the radio spectral index (Bietenholz et al. 1997). For reference, a change of 0.01 in the spectral index corresponds to a 5% change in the flux ratio between the two maps: therefore the absolute flux correction we have applied on the VLA map could contribute at most for a 0.01 on large scales, while the (conservative) 20% absolute photometric accuracy for the MPIfR bolometer array could account at most for a 0.04 offset in the spectral map. The relative photometric accuracy on smaller scales is only about 10%, and therefore spectral index variations of ~ 0.05 over distances of about $1'$, as seen in Fig. 2, cannot be ascribed to mere instrumental effects. A similar, although somehow noisier spectral map is obtained using the December 1998 data: therefore we exclude that these spectral index variations are just an effect of peculiar observing conditions.

There are two more potential sources of bias, related to instrumental characteristics. Bietenholz et al. (1997) mention a correlator nonlinearity in the radio map, that could in principle be responsible for artifacts: however they also specify that this bias may affect only angular scales $> 2.7'$, while in our spectral map most features are at smaller scales; we have also verified that the local measured spectral index may differ between regions with the same surface brightness: this cannot be accounted for as a mere effect of nonlinearity. Moreover a Gaussian convolution may not accurately reproduce the Point Spread Function (PSF) relative to the IRAM map, and in the case the radio map has been oversmoothed a slightly flatter spectrum is expected at the top of the intensity peaks: however, even by increasing by factor 50% the resolution of the the radio map with the respect to the estimated value for PSF equalization, we obtain a spectral map which is still qualitatively consistent with what shown in Fig. 2. We therefore conclude that no substantial bias derives from any of the effects discussed above.

In the following, while discussing the structure of the flatter-spectrum inner region, as well as of some steeper-spectrum elongated structures, we shall recognize the spatial coincidence with structures revealed at other wavelengths: we take these as two “a posteriori” arguments still

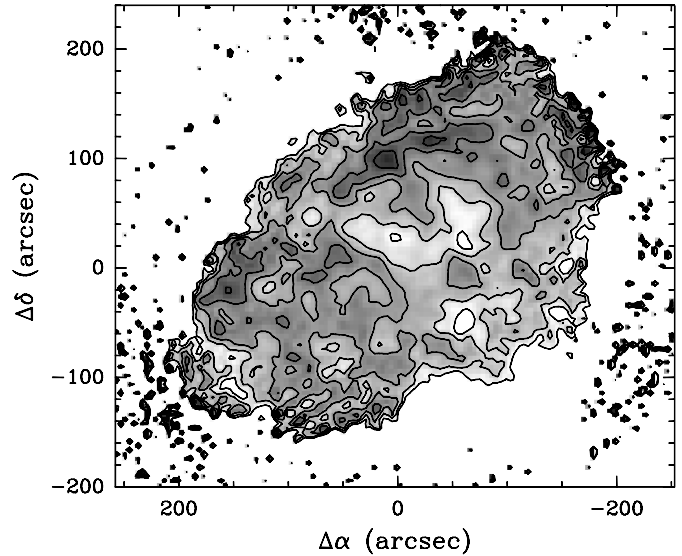


Fig. 2. Map of the spectral index α , for the 20 cm – 1.3 mm range. Contour levels range from -0.28 to -0.20 in steps of 0.02 (correspondingly the grey scale ranges from black to white).

in favour of the reality of the observed inhomogeneities in the spectral map. A final concern refers to the possibility that the comparison of observations taken at different epochs actually traces changes in time: anyway, as it will be discussed in Sect. 8, not even that effect can account for the measured spectral index inhomogeneities.

4. Evidence for the presence of additional components in the 1.3 mm map

The spectral map in Fig. 2, considered together with the radio spectral map (Bietenholz et al. 1997), indicates that in some regions of the nebula the average spectral index between 20 cm and 1.3 mm wavelengths is flatter than that at 20 cm. This means that in these regions the spectrum shows a positive second derivative (in a log-log plot) in the wavelength range between radio and millimetric (mm) wavelengths: i.e. $F(\nu) \propto \nu^{\alpha(\nu)}$ where α is increasing with ν . A similar spectrum is unusual for a single synchrotron component, unless the injection spectrum itself has a positive second derivative. The effect of synchrotron evolution is instead that of steepening the spectrum a smaller wavelengths, thus producing a spectral behaviour opposite to what we have measured.

From the spatially integrated spectrum of the Crab Nebula it is well known that a spectral break occurs at wavelengths around $20 \mu\text{m}$. Such break is commonly accepted to be an evolutive one, so that at wavelengths longer than the break the emission originates from particles whose evolution is not appreciably affected by synchrotron losses. In the case of adiabatic evolution, the particle distribution preserves its slope.

Therefore the most natural conditions leading to flatter spectra at smaller wavelengths in some regions is that, in that spectral range and in those regions, also the emission from a further population of particles is detected.

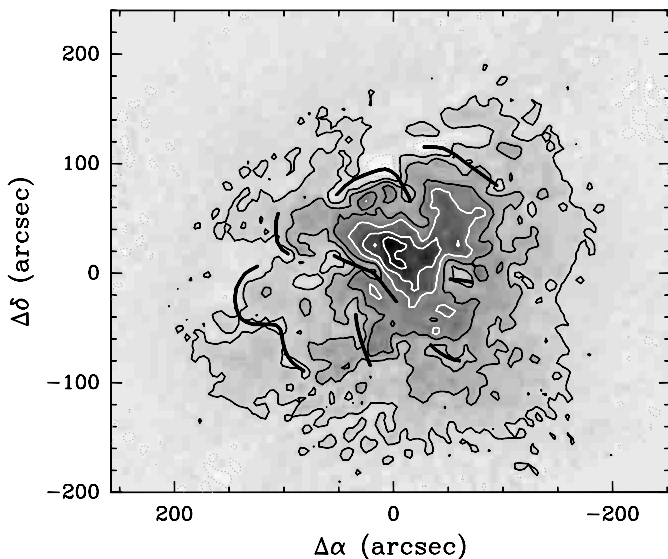


Fig. 3. Map of the residuals, after subtracting the extrapolation of the radio map with index -0.27 . The contour levels range from -0.4 to 1.7 in steps of $0.3 \text{ mJy arcsec}^{-2}$. Negative contours are indicated by dashed lines. The thick lines follow qualitatively the locations of some radio filaments (see Fig. 4), which in this map correspond to local depressions.

We shall thus attempt to map this secondary component, hereafter referred to as “component B”, while we reserve the label “A” for the component dominating in flux at radio wavelengths. With this in mind we have subtracted from our mm map an extrapolation of the radio map down to 1.3 mm , by adopting a power-law index -0.27 , as derived from multiwavelengths radio measurements of the total flux (Kovalenko et al. 1994). The map of the residuals is presented in Fig. 3: the main feature in this map is a component located in the central region of the Crab Nebula; a further component consists of some elongated features with emission depressed with respect to their surroundings. They are better visible on the N side of the nebula, where even negative values are present in the map of the residuals.

At a first glance these features may be interpreted as just a noise effect. But a more careful analysis shows that they are well correlated with the positions of synchrotron filaments, visible in the radio image. In order to settle more quantitatively this effect we have synthesized a map of the filamentary component (hereafter labelled as “f”, see Fig. 4), that together with the “amorphous” component (hereafter labelled as “a”) is responsible for the structures visible in the radio map (i.e. $\mathbf{f} + \mathbf{a} = \mathbf{A}$).

The method as well as the parameters that we have used to synthesize \mathbf{f} are described in Appendix A. They have been tuned according to the following requirements: component \mathbf{a} must look very smooth; component \mathbf{f} must instead contain mostly high spatial frequencies; negative peaks must neither appear in the map of component \mathbf{f} nor in that of \mathbf{a} ; the total flux of the filaments component must be as high as possible, within the limits set by the previous constraints. Even with these requirements some

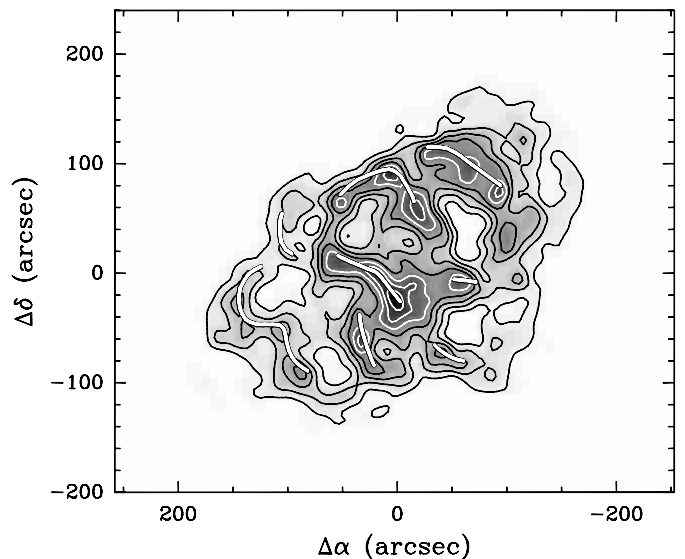


Fig. 4. Map of synchrotron filaments (component “f”), extracted from the radio map with a procedure described in Appendix A, and downgraded to $10''.5$ resolution. The contour levels range from 1.5 to 10.5 in steps of $1.5 \text{ mJy arcsec}^{-2}$. The positions of some filaments correlate with the negative features in the residual map (the thick white lines correspond to those drawn in Fig. 3).

arbitrariness is left on the choice of the procedure, but the results are not strongly dependent on this choice. The resulting map of filaments, convolved to the resolution of our 1.3 mm map, is shown in Fig. 4.

We have then estimated the relevance of the filamentary structure at 1.3 mm wavelength, by deriving the best-fit linear combination of components \mathbf{f} and \mathbf{a} , which minimizes the ripples in the residuals. The factor found for \mathbf{a} has here little meaning, because component \mathbf{a} , which accounts only for the large-scale structures, is rather insensitive to the morphological differences between component \mathbf{A} and component \mathbf{B} . Instead we shall concentrate on the best-fit factor (0.15) we have found for \mathbf{f} (this component accounts for the small scale fluctuations, and is highly sensitive to the pattern to match): its value is only $\sim 60\%$ of what expected for a pure power-law extrapolation from radio wavelengths, with a -0.27 spectral index.

The physical meaning of this deficiency will be discussed in the next section. Here we use this result just to obtain a “cleaned image” of component \mathbf{B} . The factor by which the map of component \mathbf{a} must be subtracted is however rather uncertain. As a first choice let us take an extrapolation from the radio with the canonical index -0.27 : the result is shown in Fig. 5.

According to this figure, component \mathbf{B} presents a brighter inner part, which is dominated by a feature elongated by about $1''.6$ in the NE-SW direction, and comprises two fainter extensions in the SE and NW sides, for an overall size of $1''.6$ also in that direction. This structure resembles that observed in X-rays: this point will be discussed in Sect. 6. Beyond the inner part, Fig. 5 also presents an outer halo, extending over an area of about $4' \times 5'$.

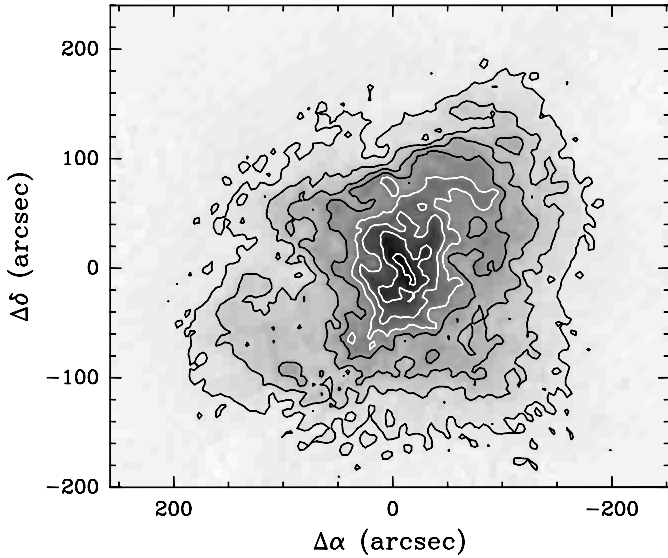


Fig. 5. Map of “component B”, after subtracting the **a** (amorphous) component, extrapolated from the radio with index -0.27 , and the **f** (filaments) component, using the best-fit factor 0.151 from the radio. The contour levels range from 0.2 to 2.3 in steps of $0.3 \text{ mJy arcsec}^{-2}$.

Uncertainties on the most appropriate factor in the subtraction of component **a** reflect into uncertainties on the structure and on the integrated flux of the halo of component **B**, while the structure of its inner part is rather insensitive to the details of the subtraction procedure. For this reason at present we can only give a coarse estimate of the total flux of this component, because dominated by its halo: on the other hand the structure of the inner part is well outlined by Fig. 5.

Using for component **a** an extrapolation from radio with index -0.27 , the estimated integrated flux of component **B** results in 59 Jy ; on the other hand -0.26 is the maximum index for which after the subtraction a positive map is left: this value is consistent both with the quoted uncertainty on the radio spectral index (0.04 ; Kovalenko et al. 1994) and with that on the 1.3 mm absolute photometry (20% , equivalent to 0.04 on the spectral index). With a -0.26 extrapolation the integrated flux of this component is measured in 54 Jy . The integrated flux of the inner part is anyway much lower: assuming that the halo emission presents a plateau in the central region, we estimate a residual flux of about 2.2 Jy .

5. Spectral bending in the filaments spectra

As mentioned in the previous section, at 1.3 mm the fluxes of the filaments are on the average 0.60 times lower than the values extrapolated from the radio data.

Our first concern has been to examine whether this is a reliable result, or if it can be just the effect of biases in the components subtraction. For instance, a spurious effect may take place if the PSF equalization between the radio and mm maps has not been carried on properly: if we have underestimated the width of the 1.3 mm PSF,

the filaments at 1.3 mm would look less prominent (relative to the amorphous component) than in the corresponding PSF-equalized radio map.

In any case such an instrumental bias cannot account for what is observed. First of all, in the case of a bias of this kind, we expect to see in the map of residuals (Fig. 3) negative peaks near the centre of the filaments, and positive residuals on the filament sides, to equilibrate the flux: but we did not measure any such effect. Even using an artificially smoothed radio map (with a PSF 50% larger than required) we still came out with basically the same result as before.

Therefore the relative weakness of the filaments in the map at 1.3 mm is a rather robust and safe result. It is in agreement also with maps of the optical continuum, in which the filaments structure is on the average much less pronounced than in the radio (Wilson 1972b).

We have found two different explanations for this effect, one based on the energy evolution of particles confined in individual filaments, and the other based on the relative efficiency of particle diffusion from filaments.

5.1. Energy evolution of confined particles

Since at radio wavelengths the spectral index of the filaments does not differ from that of the amorphous component (Bietenholz et al. 1997), the weakening of filaments at mm wavelengths could be accounted for by assuming that a spectral break intervenes in between radio and mm wavelengths.

In the case of a steady injection an evolutive break is produced at the wavelengths at which, for the emitting particles, adiabatic and synchrotron losses are comparable: in this case the expected change for the spectral index of the energy distribution is 1 (see e.g. Pacini & Salvati 1973). Let us thus model the synchrotron emission from electrons with a bi-power law energy distribution, with slopes -1.54 (in order to match the measured radio spectral index) and -2.54 respectively.

This represents a simplified case; but the further smoothing, due to the fact that the synchrotron spectrum for a single particle is broad band, causes the derived radiation spectrum to be anyway not far from what obtained with a more detailed modelling. In this way we derive for the filaments a break frequency (ν_b) of $\sim 80 \text{ GHz}$, namely a factor 200 lower than in the integrated Crab spectrum.

From this one may infer the typical magnitude of the magnetic field (B) in the filaments. If particles are confined into individual filaments the energy (E_b) corresponding to the spectral break is proportional to B^{-2} ; in turn $\nu_b \propto BE_b^2 \propto B^{-3}$: therefore filament magnetic fields are typically $\sim 200^{1/3} \sim 6$ times higher than the average nebular field. The dynamical implications of this field excess in the filaments are beyond the scope of the present work.

5.2. Particle diffusion through filaments

A very unlikely result follows if all particles are effectively diffusing through filaments. In this case E_b would be the same as in the interfilament medium and therefore $\nu_b \propto B$, leading to estimate a field in the filaments much lower than in the rest of the nebula: such a scenario, among others, would not account for the enhanced synchrotron emission in filaments, and we therefore reject it.

However particle diffusion may give more relevant effects to this problem, if the transition to the diffusive regime occurs in between radio and mm wavelengths. The diffusion time, $t_D = r_F^2/\kappa$ can be evaluated as:

$$t_D \simeq 19\,000 \text{ yr} \left(\frac{\theta_F}{1''}\right)^2 \left(\frac{B}{0.3 \text{ mG}}\right)^{3/2} \times \left(\frac{\lambda}{1.3 \text{ mm}}\right)^{1/2} \left(\frac{\kappa}{\kappa_B}\right)^{-1}, \quad (1)$$

where r_F and θ_F are respectively linear and angular transverse size of a filament (we have used 2 kpc for the distance of the Crab Nebula), $\kappa_B \simeq (m_e c^3 \gamma)/(3eB)$ (where m_e and e are respectively mass and charge of the electron, c is the speed of light and γ is the particle Lorentz factor) is the Bohm diffusion coefficient, which evaluates:

$$\kappa_B = 1.5 \times 10^{21} \text{ cm}^2 \text{ s}^{-1} \left(\frac{B}{0.3 \text{ mG}}\right)^{-3/2} \left(\frac{\lambda}{1.3 \text{ mm}}\right)^{-1/2}, \quad (2)$$

and the equation $\gamma \simeq 4.0 (m_e c^2 / eB\lambda)^{1/2}$ associates to each particle energy its typical synchrotron wavelength.

The “transition region” may be defined as the spectral region where the diffusion time is comparable with the age of the Crab Nebula, $\sim 10^3$ yr: the requirement of being located in between radio and mm wavelengths gives a constraint on transverse size, typical field and diffusion coefficient in filaments. An observable effect of diffusion is the following: if the particle density in these synchrotron filaments was originally higher than in the surroundings, a transition to a diffusive case (spanning the spectrum from long to short wavelengths) will level the particles density to that of the interfilament medium and will therefore cause a fading of the filament relative to the surrounding medium.

5.3. Limits on the diffusion coefficient

At the present stage any of the above mechanisms (either synchrotron burning or transition to diffusion) can be invoked to account for the observed filament dimming at mm wavelengths. Anyway, even in the case of a transition in the diffusion regime, the field inside filaments is required to be higher, in order to explain their brightness. We therefore suggest that synchrotron is the leading effect. But further higher resolution mm observations are required to investigate the physical conditions for individual filaments.

At any rate, the diffusion time of particles emitting at radio wavelengths (say $\lambda \sim 5$ cm) is required to be longer than the Crab Nebula age, which implies:

$$\frac{\kappa}{\kappa_B} \lesssim 100 \left(\frac{\theta_F}{1''}\right)^2 \left(\frac{B}{0.3 \text{ mG}}\right)^{3/2}. \quad (3)$$

Since typical transverse sizes of filaments are of the order of $1''$, even for fields in filaments a few times higher than the average, this upper limit on the diffusion coefficient for orthogonal diffusion in individual filaments is inconsistent with the value ($\kappa \sim 10^4 \kappa_B$) derived by comparing radial profiles at various wavelengths (Wilson 1972a; Amato et al. 2000).

Imaging of individual filaments at mm wavelengths with arcsec resolution will allow one to get more information on the origin of spectral differences between filaments and interfilament medium, on the magnetic field in individual filaments as well as on the effectiveness of particle diffusion.

6. The nature of the component B

Free-free emission definitely cannot account for component **B**. In fact a very large mass ($\sim 50 M_\odot$) of ionized matter is required to give the measured mm excess flux. In that case huge free-free emission should also appear in between infrared and optical; moreover free-free absorption should become effective at wavelengths above ~ 2 m: but none of these effects has been observed. Emission from a dust component is also unlikely (beyond the well known infrared bump at a temperature of 46 K; Strom & Greidanus 1992). In order to get the measured mm excess while maintaining the consistency with far infrared photometric data, a dust temperature lower than 5 K is required, together with a huge dust mass ($\sim 100 M_\odot$, for standard dust). These reasons, together with the fact that the map of the mm excess does not match that of the thermal mass distribution in the Crab Nebula, lead us to exclude a thermal nature for this emission.

Synchrotron emission is therefore the best candidate mechanism for component **B**, but also in this case very tight constraints on its spectrum must be set from the data. A “non-thermal” (i.e. negative) spectral index between radio and mm wavelengths can be excluded; otherwise at radio wavelengths component **B** would affect considerably the flux, hence causing spatial inhomogeneities, in the radio spectral index, above the quoted upper limits (Bietenholz et al. 1997). The data are instead consistent with a low-energy cutoff in the energy distribution of the emitting particles at a Lorentz factor $\gamma_L \sim 1.5 \times 10^4$ (for $B = 0.3$ mG).

In the next section we shall examine morphological similarities between component **B**, as extracted from the mm map, and the region with an optical spectrum flatter than the average. If this similarity is attributed to the emergence of this component at optical wavelengths and beyond, an emission spectrum with power law $\simeq -0.5$ is

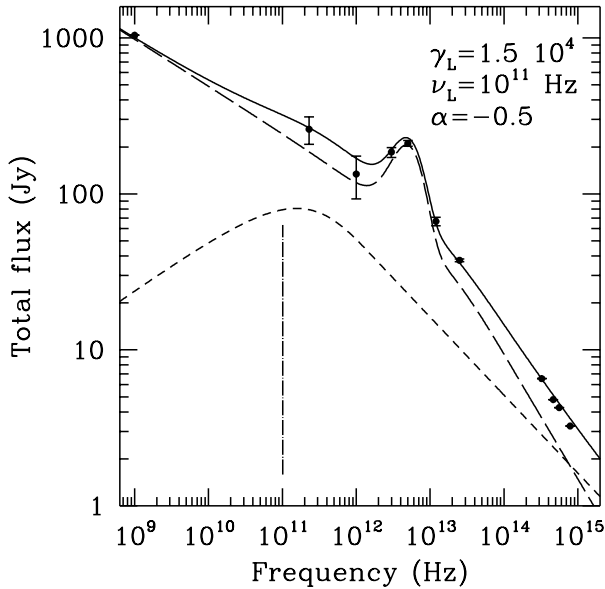


Fig. 6. A possible two-component spectral fit to photometric data from radio to optical wavelengths. Component **A** plus the dust component are represented by the long-dashed line, while the short-dashed line accounts for component **B** (the solid line showing the sum of both). The vertical dot-dashed line indicates the characteristic frequency associated with the low-energy cutoff in the particles of component **B**.

required, implying an energy distribution above γ_L consistent with a power law with index -2 . The comparison of such a spectrum with photometric data is presented in Fig. 6, with the warning that the parameters used for this model spectrum are only indicative. In this model component **A** keeps the canonical -0.27 and -0.77 slopes in radio and optical respectively (plus the known dust infrared bump): only the position of the break has been slightly refined.

The total number of emitting particles in component **B** can be estimated as:

$$N_{\text{tot}} \simeq 2 \times 10^{48} \left(\frac{F_{\text{low}}}{100 \text{ Jy}} \right) \left(\frac{B}{0.3 \text{ mG}} \right)^{-1}, \quad (4)$$

where F_{low} indicates its flux, measured near the low-energy cutoff. This number is in nice agreement with what Kennel & Coroniti (1984b) found, by fitting their wind model to the nebular spectrum between optical and X-rays: they give a rate of $2 \times 10^{38} \text{ s}^{-1}$, while N_{tot} can be roughly estimated by multiplying this rate by the Crab age, $3 \times 10^{10} \text{ s}$.

The most serious problem with otherwise successful wind models is their inability to account for the large number of radio emitting particles. The fact that the number of particles in component **B** is instead in good agreement with the Kennel & Coroniti (1984b) prediction may indicate that this mechanism is responsible for component **B**, while a different mechanism should be invoked for component **A**. Anyway a more detailed modelling, in the frame of wind models, of the spectral-spatial properties of component **B** is required in order to clarify this point.

7. Comparison with maps at other wavelengths

The morphology of component **B** (see also Fig. 7a) is substantially different from that in the radio. Except for a faint extended halo appearing in Fig. 5, but whose existence is still uncertain, component **B** is confined in a region with a size of $\sim 2'$. It does not show the SE-NW elongation, typical of the radio map; instead, its brightest feature is a narrow feature extending by about $1'$ in the NE-SW direction, from whose centre an elongated feature protrudes towards NW, while some further emission, with a broad shape, is located on its SE side.

This morphology resembles that in X-rays (shown in Fig. 7b with the same resolution), or even better that of the region of the Crab Nebula characterized by having flatter optical spectra (Fig. 7c shows the spectral map in optical). Véron-Cetty & Woltjer (1993) have in fact already noticed a similarity between the morphology of the optical spectral map and that of the X-ray emission.

What they have found can be qualitatively justified in terms of synchrotron downgrading: if the particles are injected in the central regions, the X-ray emission is confined to the inner part of the nebula because the emitting particles have short synchrotron lifetimes; for the same reason, in the outer part of the optical nebula synchrotron downgrading is responsible for the spectral softening.

Component **B**, as derived from the 1.3 mm map, now poses the following riddle: if the structure seen in X-rays and in the optical spectral map is uniquely determined by synchrotron downgrading, why a similar pattern can be also seen (after subtracting the extrapolation from the radio) in the mm spectral range, namely at wavelengths at which the emitting particles have synchrotron lifetimes much longer than the age of the nebula?

Our conclusion is that synchrotron downgrading, which must anyway be present at higher particle energies, in the Crab Nebula combines with the actual coexistence of two different particle populations (which can be recognized as component **A** and component **B**, whose spectra are shown in Fig. 6). Imaging at different wavelengths in the mm range is required in order to characterize more quantitatively the spectral properties of component **B**.

From a comparison with the radio map (Fig. 7d, again reduced to the same resolution of the mm map) it looks like the component **B** and the radio structure are anti-correlated, at least with reference to the main feature in component **B**. Further observations with higher spatial resolution will allow a better subtraction of the filaments, and a more detailed mapping of component **B**. If they will confirm that component **B** is actually located in a inner region, there where radio emitting particles (i.e. component **A**) present instead a cavity, this result would indicate that the two components are also spatially separated (with anyway a possible mixing in an intermediate region). The presence of two spatially different components would simplify the modelling of the dependence with wavelength of the Crab Nebula size; on the other hand it remains to be explained how the long-lived particles in

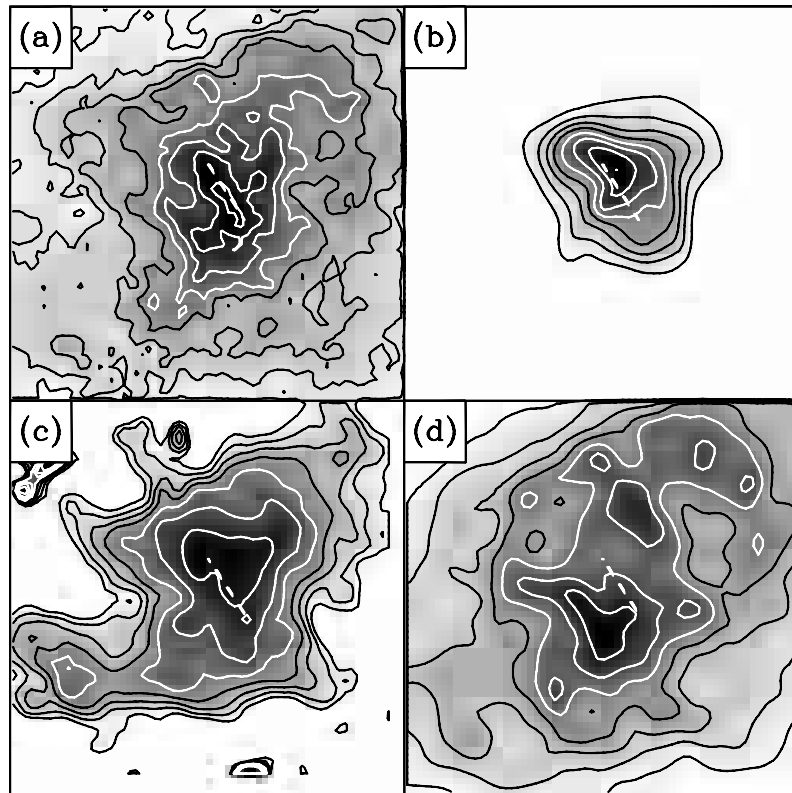


Fig. 7. Comparison of the mm map **a**) of component **B** with maps at other wavelengths (see the dashed reference line): both the X-ray map **b**) and the optical spectral map **c**) show similar patterns; the radio map **d**) seems instead anticorrelated with the main feature in component **B**. Each image is $256''$ in size.

component **B** can be effectively confined in the inner part of the Crab Nebula.

8. Effects of time variability

When discussing whether the detection of component **B** could be a mere effect of an observational bias, we have limited our analysis to instrumental effects. However the comparison for the 1.3 mm with a radio map obtained at a different epoch is not justified, if time variations of the source could account for the observed differences.

In fact short-time variability has been observed, in the Crab Nebula, in optical about the wisps region (Hester et al. 1995a) and in X-rays about the torus (Greiveldinger & Aschenbach 1999). Moreover, some small-scale wisp-like features, for which a peculiar radio spectral index had been previously quoted (Bietenholz & Kronberg 1992), have been actually discovered to vary (Bietenholz et al. 2001) with timescales of the order of one yr.

One may then wonder whether time variability may account for the changes in morphology between the radio and mm we have used, and that we have interpreted instead as due to inhomogeneities in the spectral index.

We can exclude that what we have seen is a mere effect of time variability, for various reasons. The radio variability pattern, as shown by Bietenholz et al. (2001), presents a wavy structure with near arcsec scalelength: when smeared to $10''$ resolution (as for our mm map),

the time varying structures are very likely to be averaged out completely. Moreover, our component **B** is spatially more extended than the time variable region shown by Bietenholz et al. (2001), which does not extend further than the NE-SW elongated feature in the innermost part of component **B** (see Fig. 5): even not considering its outer halo, the two extensions in the SE and NW sides do not present any noticeable radio variability.

An overall flux variability involving the inner $\sim 1/6$ of the nebula is also unlikely because such a large change would affect with ripples the secular flux evolution of the Crab Nebula, but no effect of this kind has been detected yet (Aller & Reynolds 1985). On the other hand it should be clear that synchrotron lifetimes of mm emitting particles are long, and therefore, if a detectable short-time flux increase were produced by a burst in the particle injection, this burst must inject a number of particles comparable with all particles injected in the past history of the Crab Nebula; moreover the effects of one such burst will leave for a very long time. Therefore we exclude as very remote the eventuality that time evolution be responsible of what we have interpreted as real spectral inhomogeneities.

Bietenholz et al. (2001) claim that the radio detection of dynamical structures in the same region where optical and X-ray wisps have been detected suggests a common acceleration mechanism. In a strict sense what they found is that at least “some” radio emission has the same origin as the X-ray emission: this result is consistent with ours,

since even in the case of a low-energy cutoff in the particle distribution component **B** will emit in radio, following the low-frequency $\nu^{1/3}$ synchrotron law.

At radio wavelengths it will be crucial to map the spectral index of the inner regions by using maps obtained at nearly the same time: only in this way it will be possible to tell whether all spectral inhomogeneities accounted for by Bietenholz & Kronberg (1992) are an effect of time variability, or whether the flatter spectra they found coincident to some radio wisps will be confirmed.

9. Conclusions

We have measured inhomogeneities in the spectral index between radio and mm wavelengths, and we have shown that they could be better explained in terms of the emergence of a further synchrotron component, undetected at radio wavelengths, which is located in the inner part of the nebula.

The transition in size and shape of the Crab Nebula, moving from the radio to the X-ray spectral range, is qualitatively explained in terms of synchrotron downgrading. But the fact that size and shape of component **B** at mm wavelengths resemble those seen in X-rays cannot be explained in that way, since mm emitting particles are subject to only minor synchrotron losses. We suggest instead that two different synchrotron components coexist in the Crab Nebula and that the morphological transition taking place from radio to X-rays requires a change of the relative importance of the two components.

In order to fit the data, the energy distribution of particles emitting in component **B** requires to have a low-energy cutoff. With this, the total number of particles in component **B** are in agreement with what predicted by Kennel & Coroniti (1984b) model.

Finally, in synchrotron filaments we have found the evidence for a spectral break at a frequency lower than that averaged over the whole nebula. Although there may be some effects related to particle diffusion through filaments, we take a magnetic field in filaments higher than in their surroundings as the main cause of this effect.

Acknowledgements. We wish to thank E. Amato, J. Arons, J. Hester, L. Woltjer for interesting discussions. We are grateful to M. Bietenholz for having provided us with a high quality radio map of the Crab Nebula. This work has been partly supported by the Italian Ministry for University and Research under Grant Cofin2001-02-10, and by the National Science Foundation under Grant No. PHY99-07949.

Appendix A: Procedure used to separate the filament and amorphous components

In this Appendix we describe in detail the procedure we have followed to extract from the the high-resolution map at 20 cm both the structure of the filaments network (component **f**) and that of the amorphous part (component **a**). This separation is based only on morphological criteria

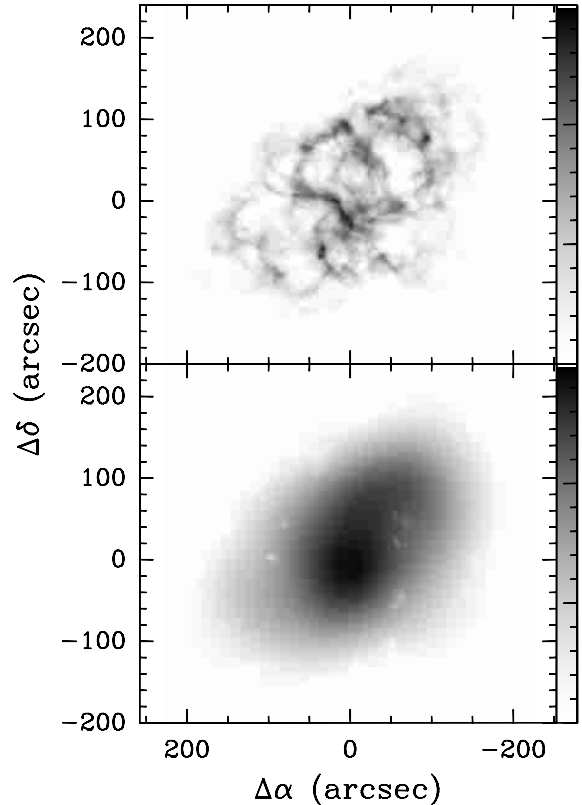


Fig. A.1. The filament (**f**; top panel) and amorphous (**a**; bottom panel) components, at full resolution, extracted from the radio map using the procedure described in the Appendix. The two maps are displayed using the same intensity levels: the grey scales, shown on the right, range from 0 to 15 mJy arcsec⁻², in steps of 1 mJy arcsec⁻². The **f** and **a** components account respectively for 30% and 70% of the total flux at 1 GHz. The map of filaments has been then downgraded to the IRAM 30-m telescope resolution (Fig. 4).

and relies on the fact that the typical scale lengths of the two components are very different. As already stated in the text, our morphological requirements are: component **a** must look very smooth; component **f** must instead contain mostly high spatial frequencies; negative peaks must appear neither in the map of component **f** nor in that of **a**; the total flux of the filaments component must be as high as possible.

A standard method to separate components characterized by different spatial frequencies is linear filtering. However this method introduces negative sidelobes, hence giving a null integrated flux for the filaments. For the extraction of the filaments contribution we have then applied a non-linear iterative procedure, with the goal of gradually “cleaning” the component **a** from **f**. We start with $\mathbf{a}_0 = M$, the original map. In each step we convolve \mathbf{a}_{i-1} by a 2-D Gaussian with a given width σ_g , and subtract the resulting image from M , using a gain G_i ; we then clip negative peaks to obtain \mathbf{f}_i and evaluate \mathbf{a}_i as $M - \mathbf{f}_i$. At the final step $G_i = 1$ is required, in order to subtract completely the filaments. We have obtained good results (Fig. A.1) with just 2 steps, using $\sigma_g = 20''$, $G_1 = 0.75$

and $G_2 = 1$. This procedure has been applied to the full resolution radio map, and only afterwards the filaments map has been convolved to the resolution of our 1.3 mm map (the final map is shown in Fig. 4).

References

- Aller, H. D., & Reynolds, S. P. 1985, *ApJ*, 293, L73
Amato, E., Salvati, M., Bandiera, R., Pacini, F., & Woltjer, L. 2000, *A&A*, 359, 1107
Atoyan, A. M. 1999, *A&A*, 346, L49
Bietenholz, M. F., & Kronberg, P. P. 1991, *ApJ*, 368, 231
Bietenholz, M. F., & Kronberg, P. P. 1992, *ApJ*, 393, 206
Bietenholz, M. F., Kronberg, P. P., Hogg, D. E., & Wilson, A. S. 1991, *ApJ*, 373, L59
Bietenholz, M. F., Kassim, N., Frail, D. A., et al. 1997, *ApJ*, 490, 291
Bietenholz, M. F., Frail, D. A., & Hester, J. J. 2001, *ApJ*, 560, 254
Greiveldinger, C., & Aschenbach, B. 1999, *ApJ*, 510, 305
Hester, J. J., Scowen, P. A., Sankrit, R., et al. 1995, *ApJ*, 448, 240
Kennel, C. F., & Coroniti, F. V. 1984a, *ApJ*, 283, 694
Kennel, C. F., & Coroniti, F. V. 1984b, *ApJ*, 283, 710
Kovalenko, A. V., Pynzar', A. V., & Udaltsov, V. A. 1994, *Astron. Rep.*, 38, 110
Kreysa, E., Gemuend, H.-P., Gromke, J., et al. 1998, *SPIE*, 3357, 319
Mezger, P. G., Tuffs, R. J., Chini, R., Kreysa, E., & Gemünd, H.-P. 1986, *A&A*, 167, 145
Pacini, F., & Salvati, M. 1973, *ApJ*, 186, 249
Strom, R. G., & Greidanus, H. 1992, *Nature*, 358, 654
Velusamy, T., Roshi, D., & Venugopal, V. R. 1992, *MNRAS*, 181, 455
Véron-Cetty, M. P., & Woltjer, L. 1993, *A&A*, 270, 370
Weiler, K. W., & Panagia, N. 1978, *A&A*, 70, 419
Wilson, A. S. 1972a, *MNRAS*, 160, 355
Wilson, A. S. 1972b, *MNRAS*, 160, 373